Metal Contaminated Sediments
Allen, H. E., editor
Chelsea, MI
Ann Arbor Press

2

METAL CYCLING IN SURFACE SEDIMENTS: MODELING THE INTERPLAY OF TRANSPORT AND REACTION

Philippe Van Cappellen and Yifeng Wang
School of Earth and Atmospheric Sciences
Georgia Institute of Technology
Atlanta, GA 30332

We are trained to think in terms of linear causality, but we need new "tools of thought": one of the greatest benefits of models is precisely to help us discover these tools and learn how to use them.

Ilya Prigogine and Isabelle Stengers [1]

1. INTRODUCTION

Surface sediments are not the passive recipients of particulate metals settling out of the water column. Rather, they act as biogeochemical reactors in which the deposited metals participate in a variety of processes, including microbial reactions, redox transformations, adsorption-desorption exchanges, and the precipitation and dissolution of minerals. These processes regulate metal speciation and, therefore, control the return of metals to the overlying aquatic environment or their retention in the underlying sediment repository (Figure 1).

The accurate description of the distributions, transformations and transport of metal species in surface sediments requires a combination of approaches and methodologies. Field-based measurements offer an integrated record of the interaction of the sedimentological, biological and geochemical processes that affect metal cycling. Laboratory studies, on the other hand, focus on the mechanisms, kinetics and equilibrium states of individual biogeochemical processes. Mathematical sediment models form the bridge between field and experimental studies.

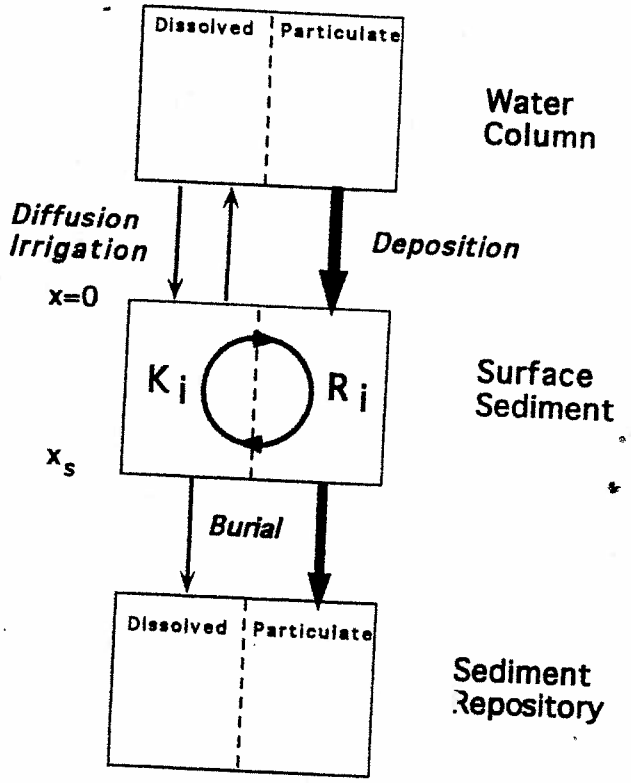

Figure 1. ***Schematic Representation of Reactions and Fluxes Regulating the Fate of Metal Species in Surface Sediments. The boundary conditions at the water-sediment interface are the bottom water composition and the particulate deposition fluxes. Within the surface sediment, the distributions of the species are modified by irreversible reactions and rapid, reversible equilibria. Solute species undergo transport via molecular diffusion, sediment mixing and irrigation. Solid species are transported by sediment accumulation and particle reworking. The coupled transport and reaction processes result in the net uptake or release of dissolved species at the water-sediment interface and in the permanent burial of particulate and dissolved species in the sediment column.***

Mathematical sediment models quantitatively describe mass transfer of metals resulting from transport and reaction. These models can be used to test the sensitivity of the system to the various transport and reaction parameters, as well as to variations in particulate deposition fluxes and bottom water composition. When properly parameterized, they allow the prediction of the response of sediment-water exchanges, porewater quality, and particulate burial fluxes to changing conditions in the overlying aquatic environment.

This paper outlines the mathematical theory of transport-reaction modeling as applied to metals in surface sediments. Based on the general theory, a model for iron and manganese in sediments is developed, and the cycling of the two metals is simulated in a number of representative depositional environments.

2. SURFACE SEDIMENTS

The most intense biogeochemical activity is concentrated within the surface layer of a sediment. This is also the portion of the sediment that directly affects the quality of the overlying water body through solute exchanges (Figure 1). The water-sediment interface constitutes the upper boundary of the surface sediment. It separates the water column, with its large-scale fluid motion and turbulent mixing, from the sediment where molecular diffusion typically dominates solute transport. For particulates, the transfer across the water-sediment interface corresponds to a transition from a relatively rapid sinking rate to a much slower sediment accumulation rate. Thus, compared to the water column, a surface sediment may be viewed as a semi-confined environment characterized by a long residence time of the particulate matter. These conditions favor the extensive biogeochemical processing of the deposited materials and the establishment of steep compositional porewater gradients.

Localizing the lower boundary of a surface sediment is less straightforward. Here, it is proposed to define this boundary as the maximum depth in the sediment at which biogeochemical reactions still exert a significant effect on solute exchanges at the water-sediment interface. Rough estimates of this depth can be obtained from a dimensional analysis of reaction and transport parameters.

Consider a reaction taking place in a given sediment layer at depth L below the water-sediment interface. Ignoring enhanced solute transport by macrofaunal activity or wave pumping, a solute produced during the reaction may still reach the water-sediment interface if $L \leq$

D_s/ω, where D_s is the bulk sediment molecular diffusion coefficient of the dissolved species (on the order of 100 $cm^2\ a^{-1}$) and ω is the linear sediment accumulation rate. In slowly depositing sediments, such as deep-sea sediments ($\omega \approx 10^{-4}$-10^{-3} cm a^{-1}), the ratio D_s/ω overestimates the thickness of the biogeochemically active layer of the sediment. In those cases, better estimates of the lower boundary of the active surface sediment are provided by the ratios ω/k or $(D_{mix}/k)^{1/2}$, where k is the pseudo-first order rate constant characterizing the "dominant" (bio)chemical reaction, usually identified as the oxidation of organic matter (see below), and D_{mix} is the sediment mixing coefficient (see section 4.4). The ratio ω/k applies to a surface sediment where advection dominates particle transport; $(D_{mix}/k)^{1/2}$ should be used when mixing dominates.

Sediment accumulation rates, sediment mixing coefficients and organic carbon oxidation rate constants vary over several orders of magnitude in marine and freshwater depositional environments [2,3]. Nonetheless, the characteristic length scales predicted by the ratios D_s/ω, ω/k or $(D_{mix}/k)^{1/2}$ - whichever applies - fall mostly within the range 10-100 centimeters. Thus, particulate matter that is buried at depths exceeding one meter may be considered to be permanently stored into the sediment repository, i.e., its further transformation no longer affects the overlying aquatic environment.

Most chemical transformations affecting metals in surface sediments are driven, directly or indirectly, by the decomposition of organic detritus deposited from the water column. Table 1 illustrates some of the changes in porewater and solid sediment chemistry brought about by organic matter degradation. The primary reactions A-1 to A-6 describe the net oxidation of organic matter, while A-7 to A-20 are secondary reactions involving the products formed during the primary oxidation reactions. The spatial and temporal distributions of these reactions control the cycling of metals in sediments.

Degradation of organic detritus deposited from the water column is the ultimate source of energy for the microbial and macrofaunal populations that inhabit the surface sediment. This "external" supply of metabolic energy maintains the overall state of chemical disequilibrium of the surface sediment. This is expressed, among other things, by the persistence of vertical gradients in chemical and biological properties in surface sediments.

Because surface sediments are open, non-equilibrium systems, a kinetic description which accounts for reaction and transport is required. Under special circumstances time-invariance may be achieved, but it will correspond to a dynamic steady-state rather than true thermodynamic equilibrium. Local equilibrium may be invoked for reactions that are

fast relative to the characteristic time scales of the transport processes. For instance, solution and surface speciation reactions are usually assumed to reach equilibrium. In general, however, the task at hand will be to provide kinetic expressions for the irreversible reactions and mass fluxes that take place in the sediment.

3. MATHEMATICAL AND NUMERICAL THEORY

Mass conservation underlies the quantitative description of sediment biogeochemistry. In its most general form, the conservation of a porewater or solid sediment constituent is given by the following partial differential equation [2,4]:

$$\frac{\partial \hat{C}}{\partial t} = \sum \nabla \bullet \hat{J} + \sum \hat{S} + \sum \hat{R} \qquad (1)$$

where t is time, $\hat{C}$ is the concentration of the constituent per unit volume of total sediment, $\nabla \bullet \hat{J}$ is the divergence of the local transport flux $\hat{J}$ affecting the constituent (e.g., sediment advection, porewater diffusion, local sediment mixing), $\hat{S}$ is a source or sink of the constituent resulting from nonlocal transport (e.g., irrigation and large scale sediment reworking), $\hat{R}$ is the rate of a biogeochemical transformation (e.g., chemical reaction, microbial production or consumption, radioactive decay).

Most data sets on sediment and porewater properties are in the form of depth profiles. Equation 1 is therefore simplified to the one-dimensional vertical case by assuming homogeneous horizontal distributions of species; and we obtain the following second-order partial differential equation:

$$\frac{\partial \zeta C}{\partial t} = \frac{\partial}{\partial x}\left\{ D\zeta \frac{\partial C}{\partial x} - \omega \zeta C \right\} + \zeta \sum S + \zeta \sum R \qquad (2)$$

where x is depth below the water-sediment interface, D is the total dispersion-diffusion coefficient (in units of surface area sediment per unit of time), and ω is the vertical sediment advection rate (in units of length sediment per unit of time). Equation 2 can be used to describe

Table 1. Irreversible Reactions (A-1 to A-19) and Alkalinity Conservation (A-20). Reactions A-1 to A-6 represent the net degradation of organic matter deposited from the water column. Reactions A-7 to A-16 describe the reoxidation of secondary species produced during the oxidation of organic matter. Reactions A-17 to A-19 correspond to the non-reductive precipitation of carbonate and sulfide mineral phases. The irreversible production or consumption of protons is buffered by the dissolved carbonate/sulfide acid-base interconversions (A-20).

$(CH_2O)_x(NH_3)_y(H_3PO_4)_z + (x+2y)O_2 + (y+2z)HCO_3^- \xrightarrow{R_1} (x+y+2z)CO_2 + yNO_3^- + zHPO_4^{2-} + (x+2y+2z)H_2O$	A-1
$(CH_2O)_x(NH_3)_y(H_3PO_4)_z + \left(\frac{4x+3y}{5}\right)NO_3^- \xrightarrow{R_2} \left(\frac{2x+4y}{5}\right)N_2 + \left(\frac{x-3y+10z}{5}\right)CO_2 + \left(\frac{4x+3y-10z}{5}\right)HCO_3^- + zHPO_4^{2-} + \left(\frac{3x+6y+10z}{5}\right)H_2O$	A-2
$(CH_2O)_x(NH_3)_y(H_3PO_4)_z + 2xMnO_2 + (3x+y-2z)CO_2 + (x+y-2z)H_2O \xrightarrow{R_3} 2xMn^{2+} + (4x+y-2z)HCO_3^- + yNH_4^+ + zHPO_4^{2-}$	A-3
$(CH_2O)_x(NH_3)_y(H_3PO_4)_z + 4xFe(OH)_3 + (7x+y-2z)CO_2 \xrightarrow{R_4} 4xFe^{2+} + (8x+y-2z)HCO_3^- + yNH_4^+ + zHPO_4^{2-} + (3x-y+2z)H_2O$	A-4
$(CH_2O)_x(NH_3)_y(H_3PO_4)_z + \frac{x}{2}SO_4^{2-} + (y-2z)CO_2 + (y-2z)H_2O \xrightarrow{R_5} \frac{x}{2}H_2S + (x+y-2z)HCO_3^- + yNH_4^+ + zHPO_4^{2-}$	A-5
$(CH_2O)_x(NH_3)_y(H_3PO_4)_z + (y-2z)H_2O \xrightarrow{R_6} \frac{x}{2}CH_4 + \left(\frac{x-2y+4z}{2}\right)CO_2 + (y-2z)HCO_3^- + yNH_4^+ + zHPO_4^{2-}$	A-6
$Mn^{2+} + \frac{1}{2}O_2 + 2HCO_3^- \xrightarrow{R_7} MnO_2 + 2CO_2 + H_2O$	A-7
$Fe^{2+} + \frac{1}{4}O_2 + 2HCO_3^- + \frac{1}{2}H_2O \xrightarrow{R_8} Fe(OH)_3 + 2CO_2$	A-8
$2Fe^{2+} + MnO_2 + 2HCO_3^- + 2H_2O \xrightarrow{R_9} 2Fe(OH)_3 + Mn^{2+} + 2CO_2$	A-9
$NH_4^+ + 2O_2 + 2HCO_3^- \xrightarrow{R_{10}} NO_3^- + 2CO_2 + 3H_2O$	A-10
$H_2S + 2O_2 + 2HCO_3^- \xrightarrow{R_{11}} SO_4^{2-} + 2CO_2 + 2H_2O$	A-11
$H_2S + 2CO_2 + MnO_2 \xrightarrow{R_{12}} Mn^{2+} + S^o + 2HCO_3^-$	A-12
$H_2S + 4CO_2 + 2Fe(OH)_3 \xrightarrow{R_{13}} 2Fe^{2+} + S^o + 4HCO_3^- + 2H_2O$	A-13
$FeS + 2O_2 \xrightarrow{R_{14}} Fe^{2+} + SO_4^{2-}$	A-14
$CH_4 + 2O_2 \xrightarrow{R_{15}} CO_2 + 2H_2O$	A-15
$CH_4 + CO_2 + SO_4^{2-} \xrightarrow{R_{16}} 2HCO_3^- + H_2S$	A-16
$Mn^{2+} + 2HCO_3^- \xrightarrow{R_{17}} MnCO_3 + CO_2 + H_2O$	A-17
$Fe^{2+} + 2HCO_3^- \xrightarrow{R_{18}} FeCO_3 + CO_2 + H_2O$	A-18
$Fe^{2+} + 2HCO_3^- + H_2S \xrightarrow{R_{19}} FeS + 2CO_2 + 2H_2O$	A-19
$CO_3^{2-} + \delta CO_2 + \delta H_2O + (1-\delta)H_2S \leftrightarrows (1+\delta)HCO_3^- + (1-\delta)HS^- \quad 0 \le \delta \le 1$	A-20

solids (C in units of mass per unit volume solid sediment) and solutes (C in units of mass per unit volume porewater solution). The reaction rate R and the nonlocal transport term S in Equation 2 are expressed in units of mass constituent per unit time and per unit volume solid sediment or porewater. The parameter ζ is related to the sediment porosity, ϕ:

$$\zeta = 1-\phi \text{ for solids}$$

$$\zeta = \phi \text{ for solutes.}$$

In Equation 2 the local transport fluxes have been separated in diffusive and advective fluxes. The diffusive processes in a sediment are molecular porewater diffusion, bulk sediment mixing, and hydrodynamic dispersion [4]. Bulk sediment mixing can result from the activity of surface dwelling and burrowing animals (bioturbation), or from the stirring action of waves and bottom currents.

Mass transfer over finite distances, during which the transported fluid or sediment is not substantially modified by small-scale mixing, is referred to as nonlocal transport. Nonlocal transport phenomena in sediments include bioirrigation (or flushing), deposit feeding, and wave pumping [5].

Analytical solutions to Equation 2 can be found for simple systems [4]. Some of the simplifying conditions include conservative behavior ($\Sigma R = 0$), steady state ($\partial\zeta C/\partial t = 0$) and the absence of nonlocal sediment reworking or irrigation ($\Sigma S = 0$). In general, however, we are interested in the time-dependent behavior of reactive, multicomponent sedimentary systems where the distributions of the various species are coupled to one another. Furthermore, nonlinear rate expressions may be required to describe certain of the microbial and geochemical processes. To solve coupled, nonlinear sets of conservation equations, numerical methods are necessary.

Standard finite-difference methods are intuitively the simplest way to numerically solve partial differential equations [6]. In one possible numerical scheme, the partial derivatives in Equation 2 are discretized as follows (only the concentration derivatives are shown):

$$\frac{\partial C}{\partial t} = \frac{C_i^{n+1} - C_i^n}{\Delta t} \qquad (3)$$

$$\frac{\partial C}{\partial x} = \theta\left\{\frac{C_i^{n+1} - C_{i-1}^{n+1}}{\Delta x} + (1-\alpha)\frac{C_{i+1}^{n+1} - C_{i-1}^{n+1}}{2\Delta x}\right\} + (1-\theta)\left\{\frac{C_i^{n} - C_{i-1}^{n}}{\Delta x} + (1-\alpha)\frac{C_{i+1}^{n} - C_{i-1}^{n}}{2\Delta x}\right\} \quad (4)$$

$$\frac{\partial^2 C}{\partial x^2} = \theta\left\{\frac{C_{i+1}^{n+1} - 2C_i^{n+1} + C_{i-1}^{n+1}}{\Delta x^2}\right\} + (1-\theta)\left\{\frac{C_{i+1}^{n} - 2C_i^{n} + C_{i-1}^{n}}{\Delta x^2}\right\} \quad (5)$$

where Δx is the grid spacing in the vertical (depth) direction and Δt is the interval between time steps; C_i^n refers to the concentration of the constituent at the *i*th grid point and at time $n\Delta t$; α and θ are adjustable parameters with values between 0 and 1.

The parameters α and θ in Equations 4 and 5 allow to experiment with various discretization schemes. The case where $\alpha = 1$ is known as the *upstream-weighted* formulation, whereas $\alpha = 0$ gives the *central-difference* formulation. With $\theta = 0$, the method is completely *explicit*, while it is completely *implicit* for $\theta = 1$. By varying α and θ it is possible to play off accuracy (which is greater for the central difference approach) *versus* numerical stability (which is usually better for upstream-weighted methods). Equations 3-5 are written for a constant grid spacing, Δx. Finite-difference schemes, however, are easily amended to incorporate variable grid spacing. In sediments, the biogeochemical transformations are usually most intense in the top few centimeters. It may, therefore, be advantageous to compress the grid spacing in the top sediment and expand it at greater depths.

The choice of a numerical scheme depends ultimately on the physical nature of the problem at hand. For example, the Crank-Nicholson scheme, with $\theta = 1/2$, is well-suited for calculating distributions that are dominated by diffusional transport. For cases where advection is the principal transport mechanism, it may be necessary to combine a large value of α with a fine grid spacing to eliminate numerical oscillations in the vicinity of sharp concentration gradients. Numerical stability analysis can guide the development of appropriate finite-difference methods through a comparison of the magnitudes of transport and reaction parameters. The presence of non-linear reaction terms and the possibility of variable transport parameters, however, complicates such an analysis. Consider, for instance, the case of a stirred surface layer overlying unstirred sediment. (The stirring of the top layer may be induced by waves and bottom currents or by

infaunal activity.) In this case, transport of solids may be dominated by random mixing in the top layer, and by sediment advection in the underlying sediment. Hence, a numerical scheme that works well for solids in the top sediment, may perform poorly at greater depths. It is therefore not surprising that designing finite difference schemes is often considered an art as much as a science.

The finite difference formulation of a transport-reaction equation of a porewater or solid sediment constituent can be transformed into a set of algebraic equations:

$$aC_{i-1}^{n+1} + bC_i^{n+1} + c_iC_{i+1}^{n+1} = d_i \qquad \text{with} \quad i = 1,2,...,N_x \quad (6)$$

where N_x is the number of grid points. The coefficients a_i, b_i, c_i, d_i in Equation 6 are functions of the sedimentation rate, the dispersion-diffusion coefficient, the sediment porosity, the nonlocal transport source strengths, the reaction rates and the finite differences Δx and Δt. The solution of the system of Equations 6 is obtained through inversion of the coefficient matrix. Efficient and high accuracy solvers for linear systems of equations abound in the literature. In the present case, the choice of an inversion algorithm is dictated by the band form of the coefficient matrix, with all the non-zero elements located on the diagonal and two adjacent codiagonals.

The rate R in Equation 2 is positive when the constituent is produced during a biogeochemical reaction and negative when the constituent is consumed. Generally speaking, rate expressions depend on the concentrations of several reactive species present in the system. For example, the rates of oxidation of dissolved Mn^{2+} and Fe^{2+} ions diffusing upward into the oxidized surface layer of a sediment depend, among others, on the dissolved metal concentration and the level of dissolved oxygen (see section 4.3). Thus, within the framework of a general sediment model, the porewater and solid sediment distributions of all reactive species must be solved simultaneously.

4. A MODEL FOR IRON AND MANGANESE IN SEDIMENTS

4.1 Reactive species

The first step in the construction of a model for Fe and Mn cycling in surface sediments is the choice of the reactive chemical species.

These may include the various dissolved, interfacial and solid forms of the metals themselves, as well as porewater and solid sediment species that affect the production or consumption of the metal species. Table 2 shows the dissolved and solid constituents used in the model. The list was kept modest, while still allowing for a realistic representation of the chemical complexity of the system.

Table 2. Dissolved and Solid Constituents. $MnCO_3$ and $FeCO_3$ may represent either the pure end-member minerals rhodocrosite and siderite, or components of a solid solution.

Dissolved Constituents	O_2
	NO_3^-
	Mn^{2+}
	Fe^{2+}
	SO_4^{2-}
	NH_4^+
	CH_4
	HCO_3^-
	HS^-
Solid Constituents	$(CH_2O)_x(NH_3)_y(H_3PO_4)_z$
	MnO_2
	$Fe(OH)_3$
	$MnCO_3$
	$FeCO_3$
	FeS

The dissolved species are represented by their total concentrations. Thus, Fe^{2+}, for example, stands for the sum of all dissolved ferrous iron species. The transport-reaction equation of a dissolved constituent written in terms of its total concentration, C_T, is,

$$\frac{\partial \phi C_T}{\partial t} = \frac{\partial}{\partial x}\left\{\sum_{i=1}^{N}\left(D_i \frac{\partial \alpha_i C_T}{\partial x}\right) - \omega \phi C_T\right\} - \phi \sum S_T + \phi \sum R_T \qquad (7)$$

where the subscript i refers to the N individual dissolved species (e.g., Fe^{2+}_{free}), $Fe(OH)^+$, Fe^{2+}-DOM, $Fe(HPO_4)^0$) that make up the total concentration, and α is the ratio of the concentration of the *i*-th species over the total concentration. The source and rate terms ΣS_T and ΣR_T describe the net production of the dissolved constituent. Thus, the homogeneous speciation reactions that transform one dissolved species of the constituent into another are not included in ΣR_T.

The phases $Fe(OH)_3$ and MnO_2 listed in Table 2 are idealized representations of the reactive, bioavailable fractions of solid Fe(III) and Mn(III, IV). Iron monosulfide, FeS, is the initial Fe(II) sulfide precipitate forming in anoxic sediments, as the result of sulfate reduction [7]. The kinetically-favored FeS is used in the model because it controls porewater iron concentrations in sulfide-rich surface sediments, rather than the thermodynamically more stable pyrite. Carbonate alkalinity production during anaerobic respiration may lead to the precipitation of carbonate minerals [2]. In freshwater sediments, relatively pure $FeCO_3$ and $MnCO_3$ may form [8]. In marine environments, the formation of solid solutions with $CaCO_3$ is more likely, especially for Mn(II) [9].

For the sake of simplicity, interfacial species of Fe and Mn are included with the solid species in the model. Adsorbed Fe and Mn species are important reaction intermediates in the redox transformations and mineral precipitation-dissolution reactions of Fe and Mn. In addition, they represent a critical component of the bioavailable fraction of the metals. Surface species can be added to the model by writing separate conservation equations for the total adsorbed concentrations of Fe and Mn. Further discussion on the inclusion of adsorption reactions in mathematical sediment models can be found elsewhere [4].

With the exception of particulate organic matter, the remaining species in Table 2 are porewater species. Taken together, the depth profiles of these species describe the vertical distribution of chemical conditions and metal speciation in the sediment.

4.2 Reactions

The decomposition of sedimentary organic matter consists of many enzymatic reactions involving a variety of organisms and a variety of intermediate compounds. Despite this complexity, it is possible to write overall degradation reactions which only take into account the

initial reactants and the final products. The overall reactions considered in the model are listed in Table 1; they include oxic respiration (A-1), denitrification (A-2), manganese oxide reduction (A-3), iron (hydr)oxide reduction (A-4), sulfate reduction (A-5), and methane formation (A-6). The reactions are listed roughly in the sequence in which they occur with increasing depth in sediments. This succession reflects the order of decreasing energy yield of the oxidation reactions for sediment heterotrophs [4].

The degradation of sedimentary organic matter is often non-stoichiometric, i.e., the relative release rates of organically-bound elements during decomposition may differ from those predicted on the basis of the elemental ratios of the total particulate organic matter [2]. This reflects the fact that sedimentary organic matter is a complicated mixture of compounds that differ in their reactivities towards degradation. The addition of biomass produced *in-situ* by bacteria and macrofauna also modifies the composition and nature of sedimentary organic detritus. Thus, the stoichiometric x:y:z ratios in reactions A-1 to A-6 of Table 1 may vary with depth and time.

The oxidation of organic matter results in the production of reduced porewater species, Mn^{2+}, Fe^{2+}, NH_4^+, HS^-, CH_4, which migrate upward in the sediment and may reoxidize when encountering more oxidizing conditions (reactions A-7 to A-13, A15 and A16). Many of these reoxidation reactions are microbially-mediated (see section 4.3). In reactions A-12 and A-13 it is assumed that elemental sulfur is the sole sulfide oxidation product. The actual situation is more complicated: additional reaction products may include polysulfides, thiosulfate and sulfate.

Reactions A-17 to A-19 in Table 1 correspond to the precipitation of carbonate and sulfide minerals. Burial of these mineral phases represent permanent sinks for reactive Fe and Mn in the sediment. Reaction A-14 accounts for the oxidation of authigenically formed FeS that is brought back up into the aerobic zone by sediment mixing.

The principal weak acids in sediments are carbonic acid and, when sulfate reduction is important, hydrogen sulfide. It is assumed in the model that the pH of porewaters is determined by the extent of dissociation of these two acids. Porewater buffering is incorporated in reactions A-1 to A-19 by assuming that protons produced or consumed in the reactions are balanced by H^+ uptake or release during rapid bicarbonate-carbonic acid inter-conversion. The reaction stoichiometries A-1 to A-19, therefore, describe the effect of the irreversible reactions on porewater alkalinity. Equilibrium reaction A-20 describes local pH balance and alkalinity conservation.

4.3 Rate laws

With the exception of reaction A-20, all reactions in Table 1 are irreversible processes and, hence, rate expressions are needed to determine their effect on porewater and solid sediment chemistry. Table 3 compiles the rate laws used in the model.

Most kinetic models for organic matter degradation in sediments derive from the simple first-order kinetic model introduced by Berner [4]:

$$R_c = -\frac{d[CH_2O]}{dt} = k_c[CH_2O]_m \qquad (8)$$

where R_c is the net rate of organic carbon oxidation, k_c is a first-order rate coefficient, $[CH_2O]$ is the concentration of organic matter, and the subscript m refers to the metabolizable fraction of the organic matter. Equation 8 states that the principal controls on the rate of oxidation of organic matter by benthic metabolism are the amount and the reactivity (or bioavailability) of the organic matter itself.

In the simplest possible case, the rate coefficient k_c in Equation 8 is assigned a single value, representative of the "average" reactivity of the sedimentary organic matter over the depth range of interest. This is the approach adopted here. More sophisticated models have been proposed which take into account the variability of organic matter reactivity with advancing degradation [2,3,10,11].

Equation 8 calculates the total rate of organic carbon oxidation. This rate can be decomposed in the contributions of the individual metabolic pathways represented by reactions A-1 to A-6 in Table 1. To this end, the fraction, f_i, of the i-th metabolic pathway is introduced:

$$f_i = \frac{R_i}{R_c} \qquad (9)$$

where R_i is the rate of carbon oxidation by reaction A-i, i = 1 to 6. At any depth and time, the following condition applies:

$$\sum_{i=1}^{6} f_i = 1 \qquad (10)$$

Table 3. Rate Laws Used in the Model; Square Brackets Denote Concentrations. See text for discussion.

$R_i = \frac{f_i}{x} k_c [CH_2O]_m$	$i = 1, ..., 6$	B-1 to B-6
$R_7 = k_7 [Mn^{2+}][O_2]$		B-7
$R_8 = k_8 [Fe^{2+}][O_2]$		B-8
$R_9 = k_9 [Fe^{2+}][MnO_2]$		B-9
$R_{10} = k_{10} [NH_4^+][O_2]$		B-10
$R_{11} = k_{11} [O_2] TS$	$TS = [HS^-] + [H_2S]$	B-11
$R_{12} = k_{12} [MnO_2] TS$		B-12
$R_{13} = k_{13} [Fe(OH)_3] TS$		B-13
$R_{14} = k_{14} [FeS][O_2]$		B-14
$R_{15} = k_{15} [CH_4][O_2]$		B-15
$R_{16} = k_{16} [CH_4][SO_4^{2-}]$		B-16
$R_{17} = k_{17} \delta_{17} \left(\frac{[Mn^{2+}][CO_3^{2-}]}{K'_{s,MnCO_3}} - 1 \right)$		B-17
$R_{18} = k_{18} \delta_{18} \left(\frac{[Fe^{2+}][CO_3^{2-}]}{K'_{s,FeCO_3}} - 1 \right)$	$\delta = 0$ for $IAP \le K'_s$ $\delta = 1$ for $IAP > K'_s$	B-18
$R_{19} = k_{19} \delta_{19} \left(\frac{[Fe^{2+}][HS^-]}{a_{H^+} K'_{s,FeS}} - 1 \right)$		B-19

To calculate the fraction f_i of a given respiratory pathway (i = 1 to 5), the model first determines whether that pathway is repressed by energetically more favorable pathways. If not, the model checks whether the rate of the i-th pathway is limited or not by the availability of the i-th external electron acceptor. The decision algorithm is based on a modified Monod or Michaelis-Menten formulation [12], which assumes that for each of the respiratory pathways there exists a critical or limiting concentration of the external oxidant. When the concentration of the oxidant exceeds the critical value, the rate of the metabolic pathway is independent of the concentration of the oxidant. Furthermore, the energetically less favorable pathways are inhibited. When the oxidant concentration drops below the critical level, the rate of the respiratory pathway becomes limited by the availability of the terminal electron acceptor, and energetically less powerful oxidants start to be utilized by the benthic heterotrophs. The computational scheme allows for a smooth transition from a zone in which a particular degradation pathway dominates another.

Application of the above approach requires a set of limiting concentrations for the successive external electron acceptors: O_2, NO_3^-, Mn(VI), Fe(III), SO_4^{2-}. Table 4 lists the ranges of the limiting concentrations reported for natural aquatic environments. In those cases where no values could be found in the literature, the ranges given in Table 4 produce depth distributions of reactive species that are comparable to measured profiles. For instance, the high limiting concentration of microbially reducible Fe(III) is consistent with the reported persistence of amorphous Fe(III) in highly reducing anoxic sediments [8,19].

The abiotic oxidation kinetics of dissolved Fe^{2+} and Mn^{2+} have been studied extensively [20,21]. These studies suggest rate laws B-7 and B-8 for the rate of oxidation of the divalent cations by oxygen. The rate coefficients k_7 and k_8 are dependent on pH and on the availability of binding sites for dissolved cations. In natural aquatic environments, oxidation of Mn^{2+} and Fe^{2+} may be microbially-mediated [22]. The limited data available suggest that the kinetics of the microbial pathways are sensitive to the same environmental parameters as the abiotic oxidation reactions. For instance, at low reactant concentrations, the microbial oxidation of Mn^{2+} correlates positively with the concentrations of dissolved Mn^{2+} and oxygen [23,24]. Equations B-7 and B-8 are, therefore, assumed to describe the rates of oxidation of Mn^{2+} and Fe^{2+} by oxygen in sediments, whether the reactions are chemical, microbiological or some combination of both. A similar bimolecular rate law is assumed for the oxidation of ferrous iron by manganese oxides.

Table 4. Limiting Concentrations of Terminal Electron Acceptors in Respiration Pathways.

Pathway	Limiting reactant	Limiting concentration	Environment	Ref.
aerobic respiration	dissolved O_2	1-10 μM	marine freshwater	12, 13
denitrification	dissolved NO_3	50-80 μM 4-20 μM	marine freshwater	14, 15 2, 13, 16
Mn reduction	solid Mn(IV)	1-10 μmol/g	marine freshwater	
Fe reduction	solid Fe(III)	1-50 μmol/g	marine freshwater	
sulfate reduction	dissolved SO_4	1600 μM 60-300 μM	marine freshwater	17 18

Studies of dissolved sulfide oxidation by oxygen suggest the empirical rate expression B-11 [25]. Existing data indicates that the oxidation rate of sulfide by Fe or Mn oxides correlates positively with the sulfide concentration and with the oxide surface areas [26,27]. Similarly, the oxidation rate of solid Fe(II) sulfides in the presence of oxygen depends on the concentration of the oxidant and the availability of mineral surface sites [28]. Because surface reactions are typically the rate determining steps in oxidative and reductive dissolution processes, the empirical rate laws may exhibit complex, non-linear dependencies on the dissolved oxidant or reductant concentration. However, for the sake of simplicity, non-unity reaction orders are not included in rate expressions B-12, B-13 and B-14.

In the absence of detailed kinetic information, the rates of nitrification (A-10) and methane oxidation (A-15 and A-16) are calculated using simple bimolecular rate Equations (B-10, B-15 and B-16).

Linear rate laws are used for the precipitation of carbonate and sulfide phases from supersaturated porewaters (B-17, B-18 and B-19). Strictly speaking, neither the rate coefficients nor the apparent solubility constants in the rate laws are true constants. These parameters depend on the compositions of porewaters and solids. In addition, the apparent rate constants vary with changes in the reactive mineral surface areas. These effects are ignored here.

4.4 Transport

Molecular diffusion coefficients of dissolved species in sediments must be corrected for sediment tortuosity, temperature, and porewater viscosity [4,29]. Temperature coefficients for the species considered in this model are listed in Table 5. For recent, unconsolidated muds the following tortuosity correction has been proposed [31]:

$$D_{sed} = \phi^2 D_{sol} \qquad (11)$$

where ϕ is the porosity, and D_{sol} and D_{sed} are the diffusion coefficients in solution and in the sediment, respectively.

Sediment reworking is frequently modeled as a random mixing process, quantified by a mixing coefficient, D_{mix}. It affects both the solid sediment and the associated porewaters. When caused by macrofauna, the process is called bioturbation. It has been shown that

Table 5. Molecular Diffusion Coefficients in Water at Infinite Dilution. The coefficients α describe the temperature dependence of the diffusion coefficients according to the formula:

$$D_o(t°C) = D_o(0°C)\{1+\alpha\ t\}$$

where t is temperature in °C. The lower part of the table gives the viscosity-based correction for calculating diffusion coefficients in seawater (35 S‰) [Ref. 29,30].

Species	D_o(0°C) in cm^2/a	α ($°C^{-1}$)
O_2	296	0.060
NO_3^-	307	0.038
Mn^{2+}	96	0.050
Fe^{2+}	106	0.044
SO_4^{2-}	156	0.045
NH_4^+	308	0.041
CH_4	235	0.052
$CO_{2,aq}$	249	0.060
HCO_3^-	169	0.048
CO_3^{2-}	137	0.047
H_2S	258	0.060
HS^-	305	0.031

Temperature (°C)	0	10	20	30
D_{sw}/D_o	0.95	0.94	0.93	0.92

in oxygenated marine depositional environments the mixing coefficient correlates positively with the sediment accumulation rate [2,42]. The reason is that a higher sedimentation rate generally corresponds to a higher deposition flux of organic matter, i.e., a larger food supply for the benthic macrofauna and, thus, a higher intensity of bioturbation. The following equation predicts macrofaunal mixing coefficients in marine environments within an order of magnitude:

$$\log D_{mix} = 1.63 + 0.851 \log \omega \qquad (12)$$

where D_{mix} is expressed in cm^2/a and ω in cm/a. The use of Equation 12 is restricted to sediments accumulating in oxic bottom waters. Benthic macrofaunal activity slows down when oxygen levels in the bottom waters drop below 30% saturation; it essentially ceases at oxygen concentrations below 0.2 ml/L [32]. Additionally, Equation 12 does not apply to areas, such as deltas and certain nearshore environments, where an extremely rapid accumulation of detrital material disrupts the establishment of a stable benthic animal population (typically, $\omega > 5$ cm/a).

The total diffusion-dispersion coefficient appearing in the transport-reaction Equation 2 includes the contributions of all random mixing processes. Thus, in a stirred sediment we have:

$$D = D_{sed} + D_{mix} \qquad \text{for a dissolved constituent}$$

$$D = D_{mix} \qquad \text{for a solid constituent}$$

In organic-rich, heavily bioturbated sediments, D_{mix} may be of the same order of magnitude as, or even exceed the molecular diffusion coefficient, D_{sed}, of dissolved species.

Changes in speciation of a dissolved constituent affect its overall diffusional flux, as can be inferred from Equation 7. If a single species dominates the speciation of a dissolved constituent over the depth range of interest, Equation 7 can be simplified to:

$$\frac{\partial \phi C_T}{\partial t} = \frac{\partial}{\partial x}\left\{\phi\left(\tilde{D}_i \frac{\partial C_T}{\partial x}\right) - \omega\phi C_T\right\} + \phi\sum S_T + \phi\sum R_T \qquad (13)$$

where $\tilde{D}$ is the dispersion-diffusion coefficient of the dominant species. When several species are important, $\tilde{D}$ is sometimes replaced in Equation 13 by the weighted dispersion-diffusion coefficient:

$$\bar{D} = \sum_{i=1}^{N} \alpha_i D_i \qquad (14)$$

This approach, however, is strictly valid only when the speciation of the constituent does not vary with depth ($\partial\alpha_i / \partial x = 0$). Although Equation 13, with $\tilde{D}$ or $\bar{D}$, is widely used by sediment modelers it must be remembered that it represents a special case of the more general transport-reaction Equation 7.

Irrigation by tube dwelling animals or wave action can cause a several-fold enhancement of the solute exchanges at the water-sediment interface [33]. A number of models for sediment irrigation have been presented in the literature [34]. The simplest nonlocal model is

$$S(x) = \alpha_x (C_o - C_x) \qquad (15)$$

where C_o and C_x are the concentrations of the constituent in the overlying water and at depth x in the sediment, α_x is the solute exchange coefficient at depth x and $S(x)$ is the irrigation source strength. Values between 2 and 300 a^{-1} have been reported for exchange coefficients in nearshore sediments [35]. Some of the highest values may in fact correspond to wave-induced irrigation rather than bio-irrigation.

4.5 Transport-reaction equations

For each constituent listed in Table 2 a transport-reaction equation is solved. Table 6 lists the equations used in the model. The constituents are coupled to one another through the reaction terms. The exception is organic carbon whose distribution in the sediment is obtained independently from any other species in the system. The equations for total dissolved carbonate (TC) and total dissolved H_2S (TS) are discussed in the next section. The goal of the simulations is primarily to investigate effects caused by chemical coupling. The set of equations is, therefore, simplified by assuming steady state and by treating sediment porosity and density as constants.

Table 6. Transport-reaction Equations. Assumptions include steady state, plus constant values for porosity, sediment accumulation rate (ω), sediment mixing coefficient (d_{mix}) and solute exchange coefficient (α_{irrig}). Symbols: ∂_t, ∂_x: time and depth partial derivatives; x_{mix}: depth of the mixed surface layer. Concentrations are expressed in mols per unit volume total sediment.

$\partial_t[CH_2O]_m = 0 = D_{solids}\partial_x^2[CH_2O]_m - \omega\partial_x[CH_2O]_m - R_C$	C-1
$\partial_t[MnO_2] = 0 = D_{solids}\partial_x^2[MnO_2] - \omega\partial_x[MnO_2] - 2xR_3 + R_7 - R_9 - R_{12}$	C-2
$\partial_t[Fe(OH)_3] = 0 = D_{solids}\partial_x^2[Fe(OH)_3] - \omega\partial_x[Fe(OH)_3] - 4xR_4 + R_8 + 2R_9 - 2R_{13}$	C-3
$\partial_t[MnCO_3] = 0 = D_{solids}\partial_x^2[MnCO_3] - \omega\partial_x[MnCO_3] + R_{17}$	C-4
$\partial_t[FeCO_3] = 0 = D_{solids}\partial_x^2[FeCO_3] - \omega\partial_x[FeCO_3] + R_{18}$	C-5
$\partial_t[FeS] = 0 = D_{solids}\partial_x^2[FeS] - \omega\partial_x[FeS] - R_{14} + R_{19}$	C-6
$\partial_t[O_2] = 0 = D_{O_2}\partial_x^2[O_2] - \omega\partial_x[O_2] + \alpha_x([O_2]_o - [O_2]) - (x+2y)R_1 - \frac{1}{2}R_7 - \frac{1}{4}R_8 - 2(R_{10} + R_{11} + R_{14} + R_{15})$	C-7
$\partial_t[NO_3] = 0 = D_{NO_3}\partial_x^2[NO_3] - \omega\partial_x[NO_3] + \alpha_x([NO_3]_o - [NO_3]) + yR_1 - \frac{(4x+3y)}{5}R_2 + R_{10}$	C-8
$\partial_t[Mn^{2+}] = 0 = D_{Mn^{2+}}\partial_x^2[Mn^{2+}] - \omega\partial_x[Mn^{2+}] + \alpha_x([Mn^{2+}]_o - [Mn^{2+}]) + 2xR_3 - R_7 + R_9 + R_{12} - R_{17}$	C-9
$\partial_t[Fe^{2+}] = 0 = D_{Fe^{2+}}\partial_x^2[Fe^{2+}] - \omega\partial_x[Fe^{2+}] + \alpha_x([Fe^{2+}]_o - [Fe^{2+}]) + 4xR_4 - R_8 - 2R_9 + 2R_{13} + R_{14} - R_{18} - R_{19}$	C-10
$\partial_t[SO_4^{2-}] = 0 = D_{SO_4^{2-}}\partial_x^2[SO_4^{2-}] - \omega\partial_x[SO_4^{2-}] + \alpha_x([SO_4^{2-}]_o - [SO_4^{2-}]) - \frac{1}{2}R_5 + R_{11} + R_{14} - R_{16}$	C-11
$\partial_t[NH_4^+] = 0 = D_{NH_4^+}\partial_x^2[NH_4^+] - \omega\partial_x[NH_4^+] + \alpha_x([NH_4^+]_o - [NH_4^+]) + y(R_3 + R_4 + R_5 + R_6) - R_{10}$	C-12
$\partial_t[CH_4] = 0 = D_{CH_4}\partial_x^2[CH_4] - \omega\partial_x[CH_4] + \alpha_x([CH_4]_o - [CH_4]) + \frac{1}{2}R_6 - R_{15} - R_{16}$	C-13
$x \le x_{mix}$: $D_{solids} = D_{mix}$ $D_i = D_{sed,i} + D_{mix}$ $\alpha_x = \alpha_{irrig}$	
$x > x_{mix}$: $D_{solids} = 0$ $D_i = D_{sed,i}$ $\alpha_x = 0$	

4.6 Alkalinity and pH

It is assumed in the model that the pH in surface sediments is buffered by the carbonate and sulfide acid-base systems. It is, therefore, useful to cast the acid-base chemistry of the porewaters in terms of the following conservative parameters:

$$TC = \left[CO_2^*\right] + \left[HCO_3^-\right] + \left[CO_3^{2-}\right] \tag{16}$$

$$TS = \left[H_2S\right] + \left[HS^-\right] \tag{17}$$

$$ALK = \left[HCO_3^-\right] + 2\left[CO_3^{2-}\right] + \left[HS^-\right] + \left[OH^-\right] - \left[H^+\right] \tag{18}$$

where TC stands for total dissolved CO_2 (CO_2^* is the sum of hydrated and unhydrated dissolved CO_2), TS for total dissolved H_2S and ALK for alkalinity. The depth distributions of the three parameters obey Equations C-14, C-15 and C-16 in Table 7. The rate expressions in the transport-reaction equations describe the production of TC, TS and ALK by the irreversible reactions A-1 to A-19.

To determine the porewater profiles of TC, TS, ALK and pH, the transport-reaction Equations C-14 to C-16 are coupled to the condition of local acid-base equilibrium (see Tables 7 and 8). Starting from an initial guess of the pH profile, Equations D-1 to D-5 are combined with C-14 and C-15 to calculate profiles of TC and TS. With this information, Equations C-16, D-6, D-7 and D-8 can be solved for the alkalinity distribution. An improved pH profile can now be derived from the equilibrium expression:

$$\left\{H^+\right\} = \frac{K_1'}{2ALK_c}\left\{(TC - ALK_c) + \left[(TC - ALK_c)^2 - 4ALK_c\frac{K_2'}{K_1'}(ALK_c - 2TC)\right]^{\frac{1}{2}}\right\} \tag{19}$$

Table 7. Pore Water Acid-base Chemistry is Calculated by Coupling the Irreversible Production and Consumption of Total Dissolved Carbonate (TC), Total Dissolved Sulfide (TS) and Alkalinity (ALK) to Local Acid-base Equilibrium. Equations D-1 to D-8 express the equilibrium species distribution in the dissolved carbonate-sulfide system. For further discussion on the dissociation constants, see Table 8.

$\partial_t(TC) = 0 = D_{CO_2}\partial_x^2(\alpha_0 TC) + D_{HCO_3^-}\partial_x^2(\alpha_1 TC) + D_{CO_3^{2-}}\partial_x^2(\alpha_2 TC) - \omega\partial_x(TC) + \alpha_x(TC_o - TC)$ $+ x(R_1 + R_2 + R_3 + R_4 + R_5) + \frac{1}{2}R_6 + R_{15} + R_{16} - R_{17} - R_{18}$	C-14
$\partial_t(TS) = 0 = D_{H_2S}\partial_x^2(\alpha_{0,S} TS) + D_{HS^-}\partial_x^2(\alpha_{1,S} TS) - \omega\partial_x(TS) + \alpha_x(TS_o - TS) + \frac{1}{2}R_5 - R_{11} - R_{12} - R_{13} + R_{16} - R_{19}$	C-15
$\partial_t(ALK) = 0 = D_{HCO_3^-}\partial_x^2(\beta_1 ALK) + 2D_{CO_3^{2-}}\partial_x^2(\beta_2 ALK) + D_{HS^-}\partial_x^2(\beta_{1,S} ALK) - \omega\partial_x(ALK) + \alpha_x(ALK_o - ALK)$ $-(x+2z)R_1 + (4x+3y-10z)/5\,R_2 + (4x+y-2z)R_3 + (8x+y-2z)R_4 + (x+y-2z)R_5 + (y-2z)R_6$ $-2(R_7 + R_8 + R_9 + R_{10} + R_{11} + R_{17} + R_{18} + R_{19}) + 2(R_{12} + 2R_{13} + R_{16})$	C-16
$\alpha_0 = \frac{[CO_2^*]}{TC} = \left(1 + \frac{K_1'}{[H^+]} + \frac{K_1'K_2'}{[H^+]^2}\right)^{-1}$	D-1
$\beta_1 = \frac{[HCO_3^-]}{ALK} = \frac{\alpha_1 TC}{(\alpha_1 + 2\alpha_2)TC + \alpha_{1,S} TS}$	D-6
$\alpha_1 = \frac{[HCO_3^-]}{TC} = \left(\frac{[H^+]}{K_1'} + 1 + \frac{K_2'}{[H^+]}\right)^{-1}$	D-2
$\beta_1 = \frac{[CO_3^{2-}]}{ALK} = \frac{\alpha_2 TC}{(\alpha_1 + 2\alpha_2)TC + \alpha_{1,S} TS}$	D-7
$\alpha_2 = \frac{[CO_3^{2-}]}{TC} = \left(\frac{[H^+]^2}{K_1'K_2'} + \frac{[H^+]}{K_2'} + 1\right)^{-1}$	D-3
$\beta_{1S} = \frac{[HS^-]}{ALK} = \frac{\alpha_{1,S} TS}{(\alpha_1 + 2\alpha_2)TC + \alpha_{1,S} TS}$	D-8
$\alpha_{0,S} = \frac{[H_2S]}{TS} = \left(1 + \frac{K_{1,S}'}{[H^+]}\right)^{-1}$	D-4
$\{H^+\}$: H^+activity	
$\alpha_{1,S} = \frac{[HS^-]}{TS} = \left(1 + \frac{[H^+]}{K_{1,S}'}\right)^{-1}$	D-5
$[CO_2^*] = [CO_{2,aq}] + [H_2CO_3]$	

Table 8. Dissociation Constants of Carbonic Acid and Hydrogen Sulfide at 1 atm. In freshwater environments, the temperature-corrected values of the thermodynamic constants (E-4 to E-6) are combined with calculated total activity coefficients. In marine environments, apparent dissociation constants are given directly by the empirical formulas E-7 to E-9. The square brackets denote total concentrations (free plus complexed species). Symbols: γ: total activity coefficient; I: ionic strength; S: salinity; Cl: chlorinity; T: absolute temperature; log = $\log_{10}$. [Ref. 36-40].

$$K_1' = \frac{[H^+][HCO_3^-]}{[CO_2^*]} = K_1 \frac{\gamma_{CO_2^*}}{\gamma_{HCO_3^-}} \quad \text{(E-1)}; \qquad K_2' = \frac{[H^+][CO_3^{2-}]}{[HCO_3^-]} = K_2 \frac{\gamma_{HCO_3^-}}{\gamma_{CO_3^{2-}}} \quad \text{(E-2)}; \qquad K_{1,S}' = \frac{[H^+][HS^-]}{[H_2S]} = K_{1,S} \frac{\gamma_{H_2S}}{\gamma_{HS^-}} \quad \text{(E-3)}$$

Thermodynamic constants:

$$-\log K_1 = -126.3405 + 6320.81/T + 45.057 \log T \qquad \text{E-4}$$

$$-\log K_2 = -90.1833 + 5143.69/T + 33.648 \log T \qquad \text{E-5}$$

$$-\log K_{1,S} = 32.55 + 1519.44/T - 15.672 \log T + 0.02722T \qquad \text{E-6}$$

Apparent constants in seawater:

$$-\log K_1' = -13.7201 + 0.031334T + 3235.67/T + 1.300\times10^{-5}(ST) - 0.1032\sqrt{S} \qquad \text{E-7}$$

$$-\log K_2' = 5371.9645 + 1.671221T + 0.22913S + 18.3802 \log(S) - 128375.28/T - 2194.3055 \log(T) - 8.0944\times10^{-4}(ST) - 5617.11 \log(S)/T + 2.136(S/T) \qquad \text{E-8}$$

$$-\log K_{1,S}' = 2.527 + 1359.96/T - 0.206S^{1/3} \qquad \text{E-9}$$

$$S(‰) = 1.80655Cl(‰)$$

$$I = 0.00147 + 0.03590Cl + 0.000068Cl^2$$

where ALK_c stands for the carbonate alkalinity, defined as:

$$ALK_c = [HCO_3^-] + 2[CO_3^{2-}] \qquad (20)$$

The procedure is iterated until convergence of all profiles.

4.7 Boundary conditions

For all solutes the upper boundary condition (x = 0) is the bottom water concentration. For solid sediment constituents, the deposition flux from the water column is specified. The flux continuity condition for a solid at the water-sediment interface is

$$F_0 = -D \frac{\partial \hat{C}}{\partial x}\bigg|_{x=0} + \omega \hat{C}_0 \qquad (21)$$

where F_0 is the deposition flux (mass per unit surface area sediment per unit time), D is the sediment reworking coefficient and $\hat{C}_0$ is the concentration of the constituent at the interface (mass per unit volume total sediment). This boundary condition is easily included in the finite-difference scheme discussed previously by using a downstream-weighted formulation for the depth derivative of $\hat{C}$ at the water-sediment interface.

The numerical calculations are performed down to a sufficiently great depth in the sediment where it may be assumed that reactions have essentially ceased. The concentration gradients of the various constituents are then set equal to zero at the lower boundary. When a sediment consists of a stirred top layer overlying a non-stirred deeper layer, additional boundary conditions are needed to insure flux continuity at the boundary separating the layers.

5. SIMULATIONS

5.1 Validation of the numerical model

A complete error analysis is beyond the scope of this paper. Nonetheless, in order to illustrate the performance of the finite

difference method, the results of numerical calculations are compared to an analytical solution. The case considered is the steady state depth distribution of organic carbon, where a single rate constant, k_c, characterizes the decomposition kinetics. The governing equation is C-1. The following set of boundary conditions applies:

$$x = 0 \qquad F_m = -D\left.\frac{\partial[CH_2O]_m}{\partial x}\right|_{x=0} + \omega[CH_2O]_{m,x=0}$$

$$x = x_{mix} \qquad \left.D\frac{\partial[CH_2O]_m}{\partial x}\right|_{x=x_{mix}} = 0 \tag{22}$$

$$x \to \infty \qquad \left.\frac{\partial[CH_2O]_m}{\partial x}\right|_{x=\infty} = 0$$

where F_m is the deposition flux of metabolizable organic carbon and x_{mix} is the depth of the stirred surface layer. The analytical solutions for the organic carbon distribution are:

$$0 \le x \le x_{mix} \qquad [CH_2O]_m = K^{-1}F_m\left\{\beta e^{\alpha(x-x_{mix})} - \alpha e^{\beta(x-x_{mix})}\right\} \tag{23}$$

$$x > x_{mix} \qquad [CH_2O]_m = K^{-1}F_m(\beta-\alpha)e^{\gamma(x-x_{mix})} \tag{24}$$

where:

$$\alpha = \frac{\omega - \sqrt{\omega^2 + 4k_cD_{mix}}}{2D_{mix}} \tag{25}$$

$$\beta = \frac{\omega + \sqrt{\omega^2 + 4k_cD_{mix}}}{2D_{mix}} \tag{26}$$

$$\gamma = \frac{k_c}{\omega} \tag{27}$$

$$K = (\beta D_{mix} - \omega)\alpha e^{-\beta x_{mix}} - (\alpha D_{mix} - \omega)\beta e^{-\alpha x_{mix}} \tag{28}$$

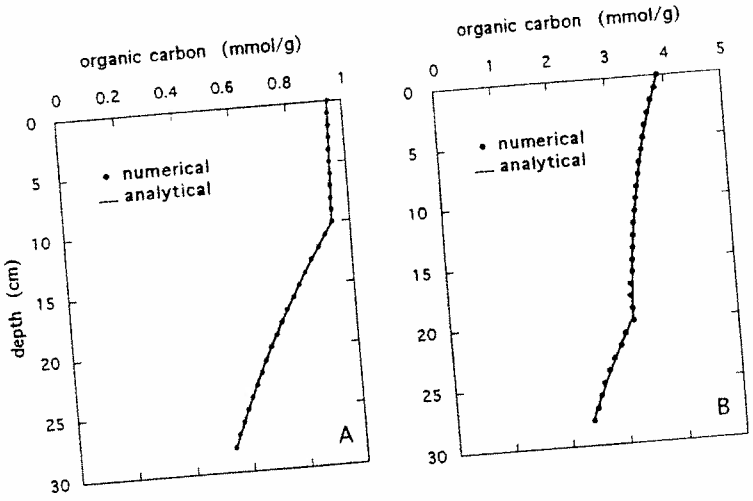

Figure 2. *Comparison of Depth Profiles of Organic Carbon Concentration Calculated with an Analytical Solution and with the Numerical, Finite-difference Method (see text). Two cases are considered: a slowly accumulating pelagic sediment (A) and a rapidly deposited, organic-rich sediment (B). Conditions: sedimentation rate (cm/a): 0.005 (A), 1.0 (B); organic carbon deposition flux (mol/cm²/a): 3×10^{-6} (A), 3×10^{-3} (B); deposited organic carbon that is metabolizable (%): 90 (A), 75 (B); rate constant of decomposition (a^{-1}): 1.5×10^{-4} (A), 0.1 (B); particle mixing coefficient (cm²/a): 0.4 (A), 40 (B); depth of mixed layer (cm): 10 (A), 20 (B); porosity (%): 80 (A & B); dry density (g/cm³): 2.5 (A & B).*

Table 9. **Environmental, Sedimentological, Biogeochemical, and Kinetic Parameters for Model Calculations of Representative Sediments. The values used were obtained from existing field-based data (for a compilation see [42]) or otherwise constrained using experimental data. Direct determinations for most of the rate constants in the table do not exist. The values reported here provide reasonable agreement between calculated and observed profiles of pore water and solid sediment properties. Much more work is needed, however, to reduce uncertainties on the numerical values of rate constants of biogeochemical processes.**

	Deep-Sea	Shelf	Coastal/ Estuarine	Oligotrophic lake	Eutrophic lake
t (°C)	2	10	18	13	13
S (‰)	35	35	20	0.005	0.007
ω (cm/a)	0.001	0.04	1	0.1	0.4
ϕ (%)	80	85	90	85	85
ρ (g/cm^3)	2.5	2.5	2.4	2.5	2.4
D_{mix} (cm^2/a)	0.1	3	10	1.0	0.01
x_{mix} (cm)	20	30	30	10	10
α (a^{-1})	0	5	10	10	0
$[O_2]_0$ (μM)	180	250	275	180	30
$[NO_3]_0$ (μM)	30	15	10	15	60
$[Mn^{2+}]_0$ (μM)	0	0	0	0	40
$[Fe^{2+}]_0$ (μM)	0	0	0	0	0.5
$[SO_4]_0$ (mM)	28	28	16	0.2	0.2
$[NH_4]_0$ (μM)	0	0	0	0	5
pH_0	8.1	8.1	7.9	7.9	7.5
Alk_0 (meq/dm^3)	2.4	2.4	5.0	1.0	5.0
TS_0 (μM)	0	0	0	0	0.2
F_c (μmol/cm^2/a)	10	100	1500	50	1000
% metabol. carbon	70	80	70	75	75
k_c (a^{-1})	0.003	0.01	0.1	0.1	0.1
x	200	200	106	150	400.
y	21	21	11	16	16
z	1	1	1	1	1
$K_m^{O_2}$(μM)	8	8	8	8	8
$K_m^{NO_3^-}$ (μM)	10	10	1	10	10
$K_m^{Mn^{IV}}$(μmol/g)	2	2	2	2	2
$K_m^{Fe^{III}}$(μmol/g)	5	5	5	5	5
$K_m^{SO_4^{2-}}$ (mM)	1	1	1	1	1
$F_{Mn^{IV}}$(μmol/cm^2/a)	4×10^{-5}	0.012	4	0.01	4
$F_{Fe^{III}}$ (μmol/cm^2/a)	1×10^{-5}	0.1	10	0.02	7
k_7 (M^{-1} a^{-1})	1×10^9	2×10^9	2×10^9	2×10^9	2×10^9
k_8 (M^{-1} a^{-1})	1×10^9	2×10^9	2×10^9	2×10^9	2×10^9
k_9 (M^{-1} a^{-1})	1×10^4	2×10^8	2×10^8	1×10^6	1×10^6
k_{10} (M^{-1} a^{-1})	1×10^7	1.5×10^7	1.5×10^7	2×10^7	2×10^7
k_{11} (M^{-1} a^{-1})	3×10^8	6×10^8	6×10^8	6×10^8	6×10^8
k_{12} (M^{-1} a^{-1})	1×10^4	1×10^4	1×10^4	1×10^4	1×10^4
k_{13} (M^{-1} a^{-1})	1×10^4	1×10^4	1×10^4	1×10^4	1×10^4
k_{14} (M^{-1} a^{-1})	2×10^7	2.2×10^7	2.2×10^7	2×10^7	2×10^7
k_{15} (M^{-1} a^{-1})	1×10^{10}	1×10^{10}	1×10^{10}	1×10^{10}	1×10^{10}
k_{16} (M^{-1} a^{-1})	1×10^{10}	1×10^{10}	1×10^{10}	1×10^{10}	1×10^{10}
k_{17} (M a^{-1})	0	1×10^{-6}	1×10^{-6}	1×10^{-6}	1×10^{-6}
k_{18} (M a^{-1})	0	1×10^{-6}	1×10^{-6}	1×10^{-6}	1×10^{-6}
k_{19} (M a^{-1})	0	5×10^{-6}	5×10^{-6}	1×10^{-6}	1×10^{-6}

The numerical solutions shown in Figure 2 were obtained using an upstream-weighted formulation for the first derivatives. An inspection of the figure shows that the finite difference calculations are virtually indistinguishable from the analytical profiles. Thus, the numerical model provides an accurate description of the organic carbon concentrations in the mixing-dominated regime of the surface layer, as well as in the advection-dominated regime of the deeper sediment. Mass is conserved across the boundary between the mixed layer and the unstirred sediment. This is an important result since an ill-designed finite difference scheme will typically betray itself in the vicinity of abrupt changes in forcing parameters.

5.2 Representative sediments

The distribution and cycling of iron, manganese and associated reactive species are simulated in a number of "representative" depositional environments. Sediment properties, bottom water conditions, deposition fluxes, transport parameters and reaction parameters for the different sediments are given in Table 9. The parameters listed are based on a broad literature survey of field-based determinations and experimental studies, combined to a comparative analysis of computed and measured depth profiles of reactive species. The latter approach is presently the sole way to obtain rate constants for many of the biogeochemical reactions taking place in natural sediments.

Computational results are presented in Figures 3 to 7 and in Table 10. The model correctly reproduces some of the major features of sedimentary biogeochemical dynamics. As observed in the real world, it is found that organic matter in deep-sea sediments is mostly degraded aerobically, while anaerobic degradation pathways, in particular sulfate reduction, dominate in organic-rich shelf and nearshore sediments [2]. Because of rapid depletion of oxygen combined with a limited availability of sulfate, most sedimentary organic matter is fermentatively degraded in sediments deposited in highly productive lakes [2].

By explicitly taking into account the reoxidation reactions of reduced species formed during the oxidation of organic matter, the model is capable of calculating what fraction of a given oxidant supplied to the sediment is directly utilized for the oxidation of organics and what fraction serves to oxidize secondary reduced species. This is illustrated in Table 10 which compares the relative importance of the various reactions reducing oxygen, Mn(III, IV) and Fe(III) in the sediments. It is apparent from the table that most dissolved oxygen consumed in deep-sea and oligotrophic lake sediments is utilized directly during

Table 10. **Representative Sediments: (1) depth-integrated rates of organic carbon oxidation and relative distribution of the various organic carbon oxidation pathways (reactions A-1 to A-6), (2) total depth-integrated rates of oxygen, manganese(IV) and iron(III) reduction, plus % of each reduction process that is coupled directly to organic carbon oxidation, (3) recycling efficiencies of iron and manganese (equation 29 in text), and (4) oxygen penetration depths.**

	Deep-Sea	Shelf	Coastal/ Estuarine	Oligotrophic lake	Eutrophic lake
C_{org} oxidation (μmol cm^{-2} a^{-1})	7	79	981	38	759
% distribution					
O_2	79.8	6.0	4.3	47.6	3.0
NO_3	10.7	5.8	1.6	9.9	9.3
Mn(IV)	2.9	0	0.1	0.2	0
Fe(III)	0.6	0.8	3.4	0.2	0.4
SO_4	6.0	87.3	90.6	4.7	0
C_{org}	0	0	0	37.3	87.3
O_2 reduction (μmol cm^{-2} a^{-1})	7	80	362	38	114
% C_{org} oxidation	93	7	14	59	21
Fe(III) reduction (μmol cm^{-2} a^{-1})	0.6	8	140	0.6	44
% C_{org} oxidation	29	34	95	50	27
Mn(IV) reduction (μmol cm^{-2} a^{-1})	0.7	4	66	0.2	19
% C_{org} oxidation	71	0	2	69	0
Recycling efficiencies (%)					
Fe	≈100	99	93	97	63
Mn	≈100	99	94	95	79
O_2 penetration (mm)*	105	12	8	25	2

* defined as the depth where the dissolved oxygen concentration drops below 1μM.

aerobic respiration. In the other cases, however, major fractions of porewater oxygen are diverted to the reoxidation of reduced species produced below the oxic surface layer. In fact, the calculations presented here suggest that this fraction dominates oxygen reduction in organic-rich shelf and coastal marine sediments, as well as in sediments of fertile freshwater environments.

Figure 3. Deep-sea Sediment. Calculated depth profiles of (a) rates of organic carbon oxidation by aerobic respiration, denitrification, Mn reduction, Fe reduction, SO_4 reduction and methanogenesis, (b) concentrations of dissolved Mn^{2+} and Fe^{2+}, (c) concentrations of Mn and Fe oxides (expressed per unit total volume sediment), (d) porewater pH, and (e) total alkalinity (Equation 18 in text) and carbonate alkalinity (Equation 20 in text). Conditions: see Table 9.

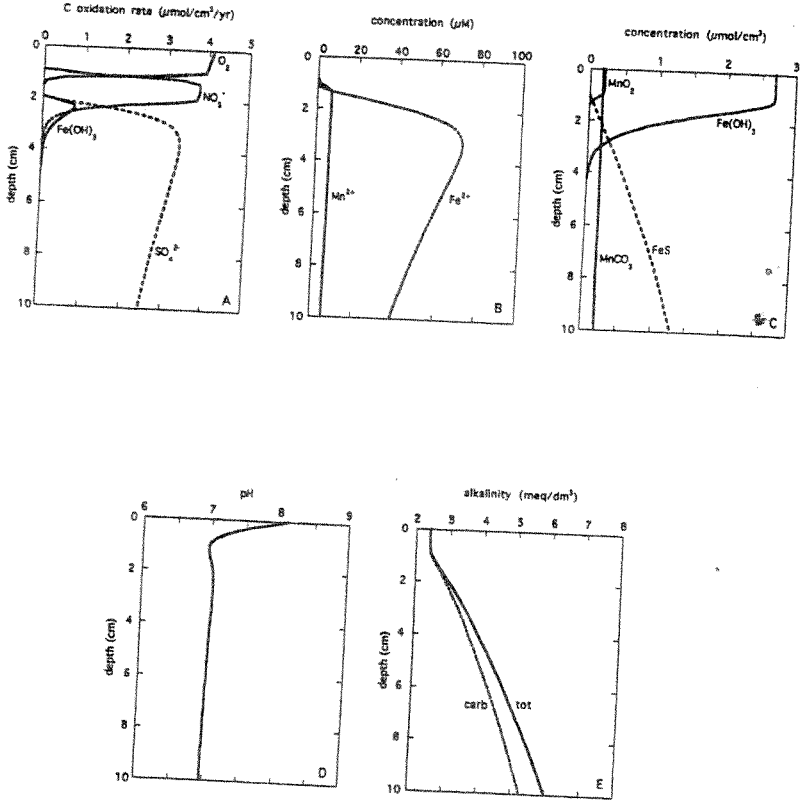

Figure 4. *Continental Shelf Sediment.*

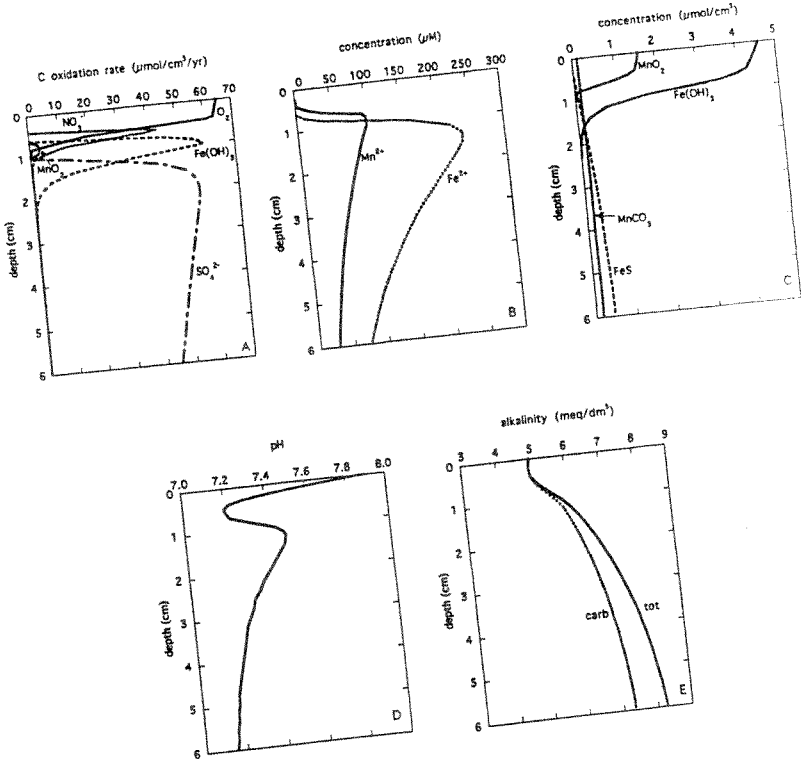

Figure 5. *Coastal-estuarine Sediment.*

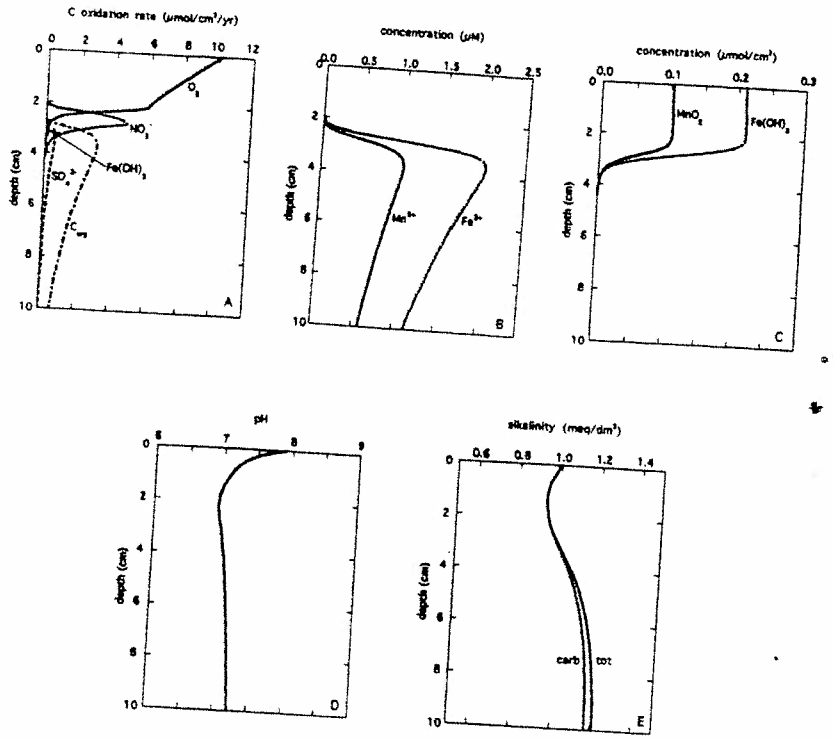

Figure 6. *Oligotrophic Lake Sediment.*

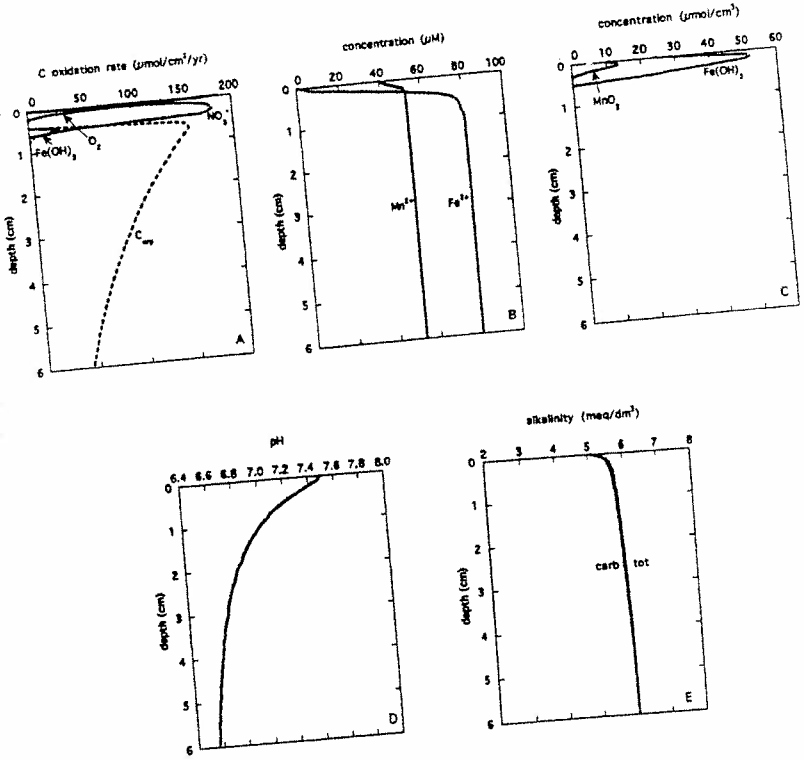

Figure 7. *Eutrophic Lake Sediment.*

The results in Table 10 allow us to compare total oxygen consumption in a sediment to the integrated organic carbon oxidation rate. With the exceptions of the coastal-estuarine and the eutrophic lake sediments, the total oxygen consumption closely approximates the total oxidation of organic carbon taking place in the sediments. Thus, in many cases the uptake rate of O_2 at the water-sediment interface should provide a reliable measure of total carbon oxidation in the sediment. However, in depositional settings characterized by oxygen-poor bottom waters and/or very high rates of organic matter oxidation this agreement breaks down. Under these circumstances, significant portions of the reduced species released to the porewaters diffuse across the water-sediment interface and are reoxidized within the overlying water column.

Dissimilatory Fe(III) reduction (reaction A-4) competes with the reduction of ferric (hydr)oxides by upward diffusing porewater sulfide (reaction A-13). According to the calculations summarized in Table 10, the partitioning of Fe(III) (hydr)oxide reduction between the dissimilatory and non-dissimilatory pathways is highly variable from one sediment to another. This reflects the variability among the various depositional settings of the relative importance of Fe(III) and sulfate reduction, as well as the ratio of the rates of organic carbon and sulfide oxidation by Fe(III) (hydr)oxides. For example, almost all Fe(III) reduction in the coastal-estuarine sediment occurs via reaction A-4 (95%), because of the very high rate of organic matter oxidation which suppresses the non-dissimilatory reduction of Fe(III). It should be noted, however, that there are still large uncertainties associated with the values assigned to the rate constant of the reaction between sedimentary Fe(III) (hydr)oxides and porewater sulfide and, therefore, the calculated distributions of dissimilatory and non-dissimilatory Fe(III) reduction given here should be considered as tentative.

As for iron, the calculated partitioning of manganese reduction between dissimilatory and non-dissimilatory pathways varies greatly among the different model sediments. In the deep-sea and oligotrophic lake sediments most Mn reduction is coupled to organic carbon oxidation, because of relatively low rates of iron reduction and, consequently, little reaction between Fe^{2+} and manganese oxides phases (reaction A-9). In contrast, manganese oxides are mainly reduced by reaction with porewater Fe^{2+} in the three other sediments. Oxidation of Fe^{2+} by Mn oxides acts as a barrier to the upward diffusion of dissolved ferrous iron cations. This reaction explains the spatial separation between the rise of porewater Mn^{2+} and that of Fe^{2+} that is often observed in sediments [8,41,43].

The net addition of oxidative capacity to sediments through the deposition of metal oxides is usually small compared to the supply of dissolved external electron acceptors from the bottom waters or to the auto-oxidative capacity of the organic matter itself. However, because Fe and Mn undergo redox cycling in sediments covered by oxygen-containing bottom waters, the contribution of the metal oxides to the oxidation of sedimentary organic matter plus secondary reduced species may be much larger than would be predicted from the oxide deposition fluxes alone [41]. At steady state, a measure of the importance of redox cycling of Fe or Mn in a sediment is given by the recycling efficiency, E:

$$E_i = \frac{\int R_{ox,i}dx}{\int R_{red,i}dx} = 1 - \frac{F_i}{\int R_{red,i}dx} \qquad (29)$$

where the integrals represent the total, depth-integrated rates of oxidation or reduction of Mn and Fe, and F_i is the deposition flux of the metal oxide at the water-sediment interface. The value of E varies from 0 to 1. The lower boundary corresponds to the case where each deposited metal cation undergoes a single reduction before it is lost from the surface sediment, either through burial into the sediment repository or diffusion back to the water column. Non-zero values of E indicate that the metal cations are cycled several times among their redox states before being lost from the surface sediment. The average number of times an iron or manganese cation cycles through its oxidized and reduced forms is given by 1/(1-E).

Values for the recycling efficiencies of Fe and Mn in the different model sediments are given in Table 10. The lowest values of E are found in the eutrophic lake sediment, where the thin oxic surface layer cannot prevent the escape of significant fractions of the reduced metal cations to the overlying water column. In the other sediments, the recycling efficiencies are much higher, approaching 100% in shelf and deep-sea sediments. The somewhat lower values of E in the coastal-estuarine sediment are due to the relatively more important precipitation and burial of reduced iron and manganese mineral phases in this environment.

Redox cycling of iron and manganese within a sediment may cause a build-up of the oxide-bound metal concentrations in the oxidized portion of the sediment. This is most clearly illustrated by the deep-sea sediment where the oxic-anoxic boundary acts as a quasi-perfect trap for dissolved metal cations. In the absence of redox cycling, the concentrations of reactive Fe and Mn oxides in the top part of this

sediment should not exceed a few hundredths of μmol/cm^3. The calculated concentrations, however, are several orders of magnitude higher (Figure 3b), because of the upward redistribution by particle mixing of metal oxides precipitated within the oxic to anoxic transition zone.

The concentrations and cycling of reactive Fe and Mn species in sediments depend on the magnitudes of particle and fluid transport. This is illustrated in Figure 8 where the recycling efficiencies and the maximum observed metal oxide concentrations in the coastal-estuarine sediment are plotted as a function of the particle mixing coefficient. The recycling efficiencies are only slightly affected by changes in the biodiffusion coefficient. Large differences, however, are observed in the absolute concentrations of metal oxides. Lower biodiffusion coefficients correspond to a less rapid removal of the oxides from the oxidation fronts and, hence, higher and sharper maxima in the metal oxide depth profiles.

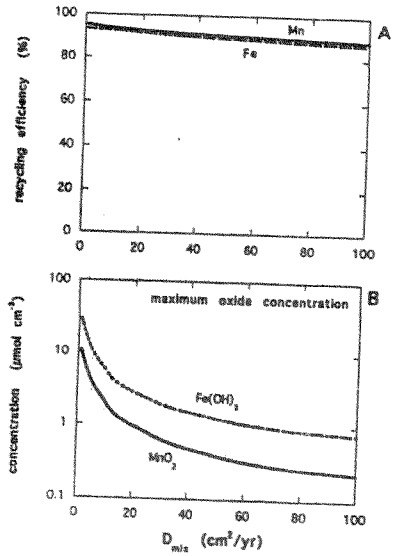

Figure 8. ***Effect of the Particle Mixing Coefficient on (a) the Recycling Efficiencies of Mn and Fe and (b) the Maximum Concentrations of Mn and Fe Oxides in the Coastal-estuarine Sediment. All other conditions are the same as in Figure 5.***

The simulations in Figure 8 emphasize two important features of sediment biogeochemical dynamics. First, in complex transport-reaction systems such as sediments there may not exist a simple relationship between the concentration of a given reactive species and its rate of biogeochemical transformation. Second, in order to predict the behavior, speciation and retention of metals in sediments, one requires a quantitative understanding of, not only the chemistry and biochemistry involved, but also the physical transport processes.

Porewater pH and alkalinity are sensitive indicators of sediment biogeochemistry. Figures 3 to 7 show that each model sediment has its own characteristic pH and alkalinity signature. Typically, the pH of the porewaters drops below the water-sediment interface, reflecting acid production as a result of O_2 reduction [44]. In the eutrophic lake sediment this decreasing trend persists below the aerobic layer as denitrification and methanogenesis take over as the major processes of organic matter degradation. In the coastal-estuarine and in the shelf sediment, however, the pH reaches a minimum at the base of the aerobic layer, followed by an increase. The observed pH maximum coincides with the alkalinity production during Mn and Fe reduction coupled to organic carbon and porewater sulfide oxidation (reactions A-3, A-4, A-12 and A-13). Below the maximum, porewater pH decreases again with depth. This decrease is driven mainly by the release of protons during the precipitation of hydrogen sulfide with ferrous iron (reaction A-19). For sufficiently low sulfide precipitation rates the pH may actually continue to rise with depth as observed, e.g., in [45].

The features of the pH profile, e.g., the pH minimum and maximum described above for the coastal-estuarine sediment, are sensitive to the relative importance of the various redox reactions taking place. For instance, comparatively more hydrogen ions are produced per O_2 molecule during the oxidation of Mn^{2+} and Fe^{2+} ions (reactions A-7 and A-8) than during aerobic respiration (reaction A-1). Thus, well-developed metal oxidation fronts in sediments may be expected to be associated with pronounced pH minima. Similarly, the magnitude and width of the pH maximum observed in Figure 7d is sensitive to the relative contributions of metal oxides and oxygen to the oxidation of sulfide diffusing up from the sulfate reduction zone.

As was pointed out several times during the previous discussion, sediment redox chemistry offers many examples of multiple pathways competing for the same species. The fact that these pathways often have different effects on porewater alkalinity and pH offers one potential avenue for evaluating the contributions of the different pathways (compare, for instance, the stoichiometries of the sulfide oxidation reactions A-11, A-12 and A-13). Technological advances in the last

decade have produced microelectrodes that permit the measurement of depth profiles of pH and other porewater properties with spatial resolutions inferior to a millimeter. We foresee that the combination of micro-profiling of porewaters and modeling of the type presented in this paper will resolve many of the questions about the detailed biogeochemistry of surface sediments that until recently may have seemed intractable.

6. CONCLUSIONS

The development of coupled, multi-component transport-reaction models that simulate the behavior of metals and associated reactive species in surface sediments has been made possible in the last decades by the rapidly increasing accessibility to powerful workstations and personal computers. In this paper, we have tried to show that despite the complexity of sediment biogeochemistry, the fundamental transport-reaction theory and its implementation into numerical computer codes is relatively straightforward. In fact, the construction of realistic biogeochemical models for surface sediments is presently limited by our ability to identify, formalize and parameterize the individual transport and reaction processes, rather than by inadequate computational and mathematical tools.

Acknowledgments: The authors acknowledge the fruitful discussions with Don Canfield on the cycling of Fe and Mn in sediments. They wish to thank Alakendra Roychoudhury for his help in developing the sediment model presented in this paper. Through their support, their willingness to share data and expertise, or by providing inspiration, the following people also deserve our gratitude: Bob Berner, Jean-François Gaillard and Tracey Tromp. This research was funded by the U.S. Environmental Protection Agency under Cooperative Agreement No. 820813, administered through the Environmental Research Laboratory, Athens, Georgia.

REFERENCES

1. Prigogine, I. and I. Stengers, *Order out of Chaos: Man's New Dialogue with Nature* Bantam Books, (New York, 1984).

2. Van Cappellen, P., J.-F. Gaillard and C. Rabouille, "Biogeochemical Transformations in Sediments: Kinetic Models of Early Diagenesis," in *Interactions of C, N, P and S Biogeochemical Cycles and Global Change*, R. Wollast, F.T. Mackenzie and L. Chou, Eds., pp. 401-445 Springer-Verlag, (Berlin, 1993).

3. Middelburg, J.J., "A Simple Rate Model for Organic Matter in Marine Sediments," *Geochim. Cosmochim. Acta* 53:1577-1581 (1989).

4. Berner, R.A., *Early Diagenesis: A Theoretical Approach* Princeton Univ. Press, (Princeton, 1980).

5. Boudreau, B.P., "Mathematics of Tracer Mixing in Sediments: II. Nonlocal Mixing and Biological Conveyor-Belt Phenomena," *Amer. J. Sci.* 286:199-238 (1986).

6. Lapidus, L. and G.F. Pinder, *Numerical Solution of Partial Differential Equations in Science and Engineering* John Wiley and Sons, (New York, 1982).

7. Berner, R.A., "Sedimentary Pyrite Formation: An Update," *Geochim. Cosmochim. Acta* 48:605-615 (1984).

8. Wersin, P., P. Höhener, R. Giovanoli and W. Stumm, "Early Diagenetic Influences on Iron Transformations in a Freshwater Lake Sediment," *Chem. Geol.* 90:233-252 (1991).

9. Mucci, A., "Manganese Uptake during Calcite Precipitation from Seawater: Conditions Leading to the Formation of a Pseudokutnahorite," *Geochim. Cosmochim. Acta* 52:1859-1868 (1988).

10. Boudreau, B.P. and B.R. Ruddick, "On a Reactive Continuum Representation of Organic Matter Diagenesis," *Amer. J. Sci.* 291:507-538 (1991).

11. Burdige, D.J., "The Kinetics of Organic Matter Mineralization in Anoxic Marine Sediments," *J. Mar. Res.* 49:727-761 (1991).

12. Gaillard, J.-F. and C. Rabouille, "Using Monod Kinetics in Geochemical Models of Organic Carbon Mineralization in Deep-Sea Surficial Sediments," in *Deep-Sea Food Chains and the Global Carbon Cycle*, G.T. Rowe and V. Pariente, Eds., pp. 309-324 Kluwer Academic Publ., (The Netherlands, 1992).

13. Nielsen, L.P., P.B. Christensen, N.P. Revsbech and J. Sørensen, "Denitrification and Oxygen Respiration in Biofilms Studied with a Microsensor for Nitrous Oxide and Oxygen," *Microb. Ecol.* 19:63-72 (1990).

14. Billen, G., "A Budget of Nitrogen Recycling in North Sea Sediments Off the Belgian Coast," *Estuarine Coastal Mar. Sci.* 7:127-146 (1978).

15. Esteves, J.L., G. Mille, F. Blanc and J.C. Bertrand, "Nitrate Reduction Activity in a Continuous Flow-through System in Marine Sediments," *Microb. Ecol.* 12:283-290 (1986).

16. Murray, R.E., L.L. Parson and M.S. Smith, "Kinetics of Nitrate Utilization by Mixed Populations of Denitrifying Bacteria," *Appl. Environ. Microbiol.* 55:717-721 (1989).

17. Boudreau, B.P. and J.T. Westrich, "The Dependence of Bacterial Sulfate Reduction on Sulfate Concentration in Marine Sediments," *Geochim. Cosmochim. Acta* 48:2503-2516 (1984).

18. Ingvorsen, K., A.J.B. Zehnder and B.B. Jørgensen, "Kinetics of Sulfate and Acetate Uptake by *Desulfobacter postgatei*," *Appl. Environ. Microbiol.* 47:403-408 (1984).

19. Lovley, D.R., "Organic Matter Mineralization with the Reduction of Ferric Iron: A Review," *Geomicrobiol. J.* 5:375-399 (1987).

20. Morgan, J.J., W. Sung and A. Stone, "Chemistry of Metal Oxides in Natural Water: Catalysis of the Oxidation of Manganese(II) by γ-FeOOH and Reductive Dissolution of Manganese(III) and (IV) Oxides," in *Environmental Inorganic Chemistry*, K.J. Irgolic and A.E. Martell, Eds., pp. 167-184 VCH Publishers, Inc., (Weinheim, Germany 1985).

21. Wehrli, B., "Redox Reactions of Metal Ions at Mineral Surfaces," in *Aquatic Chemical Kinetics*, W. Stumm, Ed., pp. 311-336 John Wiley and Sons, (New York, 1990).

22. Emerson, S., S. Kalhorn, L. Jacobs, B.M. Tebo, K.H. Nealson and R.A. Rosson, "Environmental Oxidation Rate of Manganese(II): Bacterial Catalysis," *Geochim. Cosmochim. Acta* 46:1073-1079 (1982).

23. Kepkay, P.E., D.J. Burdige and K.H. Nealson, "Kinetics of Bacterial Manganese Binding and Oxidation in the Chemostat," *Geomicrobiol. J.* 3:245-262 (1984).

24. Tebo, B.M. and S. Emerson, "Effect of Oxygen Tension, Mn(II) Concentration, and Temperature on the Microbially Catalyzed Mn(II) Oxidation Rate in a Marine Fjord," *Appl. Environ. Microbiol.* 50:1268-1273 (1985).

25. Morse, J.W., F.J. Millero, J.C. Cornwell and D. Rickard, "The Chemistry of Hydrogen Sulfide and Iron Sulfide in Natural Waters," *Earth-Science Rev.* 24:1-42 (1987).

26. Pyzik, A.J. and S.E. Sommer, "Sedimentary Iron Monosulfides: Kinetics and Mechanism of Formation," *Geochim. Cosmochim. Acta* 45:687-698 (1981).

27. Yao, W. and F.J. Millero, "The Rate of Sulfide Oxidation by δMnO_2 in Seawater," *Geochim. Cosmochim. Acta* 57:3359-3365 (1993).

28. Moses, C.O., D.K. Nordstrom, J.S. Herman and A.L. Mills, "Aqueous Pyrite Oxidation by Dissolved Oxygen and by Ferric Iron," *Geochim. Cosmochim. Acta* 51:1561-1571 (1986).

29. Lerman, A., *Geochemical Processes: Water and Sediment Environments* John Wiley and Sons, (New York, 1979).

30. Ullman, W.J. and R.C. Aller, "Diffusion Coefficients in Nearshore Marine Sediments," *Limnol. Oceanogr.* 27:552-556 (1982).

31. Li, Y.-H and S. Gregory, "Diffusion of Ions in Sea Water and in Deep-Sea Sediments," *Geochim. Cosmochim. Acta* 38:703-714 (1974).

32. Tyson, R.V. and T.H. Pearson, "Modern and Ancient Continental Shelf Anoxia: An Overview," in *Modern and Ancient Continental Shelf Anoxia*, R.V. Tyson and T.H. Pearson, Eds., pp. 1-24 Geological Society Special Publication 58, (London, 1991).

33. Christensen, J.P., A.H. Devol and W.M. Smethie, Jr., "Biological Enhancement of Solute Exchange Between Sediments and Bottom Water on the Washington Continental Shelf," *Continental Shelf Res.* 3:9-23 (1984).

34. Boudreau, B.P., "On the Equivalence of Non-Local and Radial-Diffusion Models for Porewater Irrigation," *J. Mar. Res.* 42:731-735 (1984).

35. Emerson S., R. Jahnke and D. Heggie, "Sediment-Water Exchange in Shallow Water Estuarine Sediments," *J. Mar. Res.* 42:709-730 (1984).

36. Stumm, W. and J.J. Morgan, *Aquatic Chemistry* John Wiley and Sons, (New York, 1981).

37. Mehrbach, C., C.H. Culberson, J.E., Hawley and R.M. Pytkowicz, "Measurement of the Apparent Dissociation Constants of Carbonic Acid in Seawater at Atmospheric Pressure," *Limnol. Oceanogr.* 18:897-907 (1973).

38. Millero, F.J., "The Thermodynamics of the Carbonate System in Seawater," *Geochim. Cosmochim. Acta* 43:1651-1661 (1979).

39. Goldhaber, M.B. and I.R. Kaplan, "Apparent Dissociation Constants of Hydrogen Sulfide in Chloride Solutions," *Marine Chem.* 3:83-104 (1975).

40. Millero, F.J., "The Thermodynamics and Kinetics of the Hydrogen Sulfide System in Natural Waters," *Marine Chem.* 18:121-147 (1986).

41. Canfield, D.E., B. Thamdrup and J.W. Hansen, "The Anaerobic Degradation of Organic Matter in Danish Coastal Sediments: Iron Reduction, Manganese Reduction, and Sulfate Reduction," *Geochim. Cosmochim. Acta* 57:3867-3883 (1993).

42. ~~Tromp, T.K., P. Van Cappellen and R.M. Key, "Early Diagenesis of Organic Carbon and Organic Phosphorus in Marine Sediments: I. The Model," *Geochim. Cosmochim. Acta* (in press, 1994).~~

43. Froelich, P.N., G.P. Klinkhammer, M.L. Bender, N.A. Luedtke, G.R. Heath, D. Cullen, P. Dauphin, D. Hammond, B. Hartman and V. Maynard, "Early Oxidation of Organic Matter in Pelagic Sediments of the Eastern Equatorial Atlantic: Sub-oxic Diagenesis," *Geochim. Cosmochim. Acta* 43:1075-1090 (1979).

44. Boudreau, B.P., "Modelling the Sulfide-Oxygen Reaction and Associated pH Gradients in Porewaters," *Geochim. Cosmochim. Acta* 55:145-159 (1991).

45. Jahnke, R.A., "Early Diagenesis and Recycling of Biogenic Debris at the Seafloor, Santa Monica Basin, California," *J. Mar. Res.* 48:413-436 (1990).

42. Tromp, T. K., P. Van Cappellen and R. M. Key, "A Global Model for the Early Diagenesis of Organic Carbon and Organic Phosphorus in Marine Sediments," Geochim. Cosmochim. Acta 59:1259-1284 (1995)